Composites Part A 120 (2019) 106–115

Contents lists available at ScienceDirect

Composites Part A

journal homepage: www.elsevier.com/locate/compositesa

Static and fatigue interlaminar shear reinforcement in aligned carbon nanotube-reinforced hierarchical advanced composites

Xinchen Ni[a], Carolina Furtado[c,d], Estelle Kalfon-Cohen[b], Yue Zhou[b], Gabriel A. Valdes[a], Travis J. Hank[b], Pedro P. Camanho[c,d], Brian L. Wardle[b,*]

[a] Department of Mechanical Engineering, Massachusetts Institute of Technology, Cambridge, MA 02139, USA
[b] Department of Aeronautics and Astronautics, Massachusetts Institute of Technology, Cambridge, MA 02139, USA
[c] DEMec, Faculdade de Engenharia da Universidade do Porto, Rua Dr. Roberto Frias, s/n, 4200-465 Porto, Portugal
[d] INEGI, Instituto de Ciência e Inovação em Engenharia Mecânica e Engenharia Industrial, Rua Dr. Roberto Frias, 400, 4200-465 Porto, Portugal

ARTICLE INFO

Keywords:
Carbon nanotubes
Nano-engineered
Strength
Fatigue

ABSTRACT

High densities (>10 billion fibers per cm^2) of aligned carbon nanotubes (A-CNTs) are used to reinforce the interlaminar resin-rich region of aerospace-grade unidirectional carbon microfiber plies in a hierarchical carbon fiber reinforced plastic (CFRP) laminate architecture. Such nano-engineered interfaces have been shown to increase interlaminar fracture toughness and substructural in-plane strengths, and here we show a 115% average increase in fatigue life across all load levels (60–90% of static strength), with a larger increase of 249% in high-cycle (at 60% of static strength) fatigue, despite no statistically significant increase in static strength. These findings are in agreement with a numerical damage progression model developed to simulate both interlaminar and intralaminar damage in the laminates, which shows the relative insensitivity of short-beam shear (SBS) strength to the enhancement of interlaminar fracture toughness, *e.g.*, a 50% increase in interlaminar toughness yields an SBS strength increase of less than 20%. Consistent with observations of other CNT-reinforced epoxy architectures, larger improvements in fatigue life are noted in low-stress regimes (*e.g.,* high-cycle fatigue) vs. in high-stress regimes (*e.g.,* static and low-cycle fatigue), indicating a transition in dominant mechanisms from high-energy dissipation caused by CNT pullout to low-energy dissipation caused by CNT fracture as stress increases.

1. Introduction

A fundamental limitation in advanced composite materials is the poor through-thickness mechanical strength due to the resin-rich region at ply interfaces, which makes the laminate particularly susceptible to delamination and related failure modes [1]. Different methodologies have emerged to provide reinforcement in the laminate through-thickness, or z-direction, including stitching, z-pinning, and 3D weaving [2–8]. However, a common drawback of these existing approaches is that they use pins and stitches that are large relative to the structural fibers (microfibers) of the composite, causing unavoidable artifacts during manufacturing, including microfiber movement and damage, in-plane microfiber volume loss and resin-rich areas. As a result, laminate in-plane properties are often significantly reduced [2]. In very recent years, interest has grown in using nanomaterials as second-phase fillers for enhancement of strength and toughness of advanced composites [9–15]. One of the major advantages of using nano-scale reinforcements, particularly carbon nanotubes (CNTs), is that they possess excellent properties comparable to, or better than carbon microfibers, and their small size relative to the advanced microfibers could reinforce the laminates without degrading the in-plane properties [15–17], and positive scale effects in bridging toughening have been identified [18–20]. In addition, the exceptional thermal [21–26] and electrical [25–27] properties of CNTs enable multifunctionality in composite structures [14,28–30].

The most common practice to incorporate CNTs in composites is by mixing them with the matrix, followed by infusion or impregnation of the microfibers with the CNT-modified matrix. This process is simple and largely compatible with existing composite manufacturing processes, but it is limited to very low CNT loading fractions (<1%) because the resin viscosity greatly increases by the addition of CNTs, reducing the processability of the matrix through agglomeration, filtering, and other effects [15]. Current methods to increase CNT loading include high-speed mixing, surface functionalization, and

* Corresponding author.
E-mail address: wardle@mit.edu (B.L. Wardle).

https://doi.org/10.1016/j.compositesa.2019.02.023
Received 20 October 2018; Received in revised form 22 February 2019; Accepted 24 February 2019
Available online 25 February 2019
1359-835X/

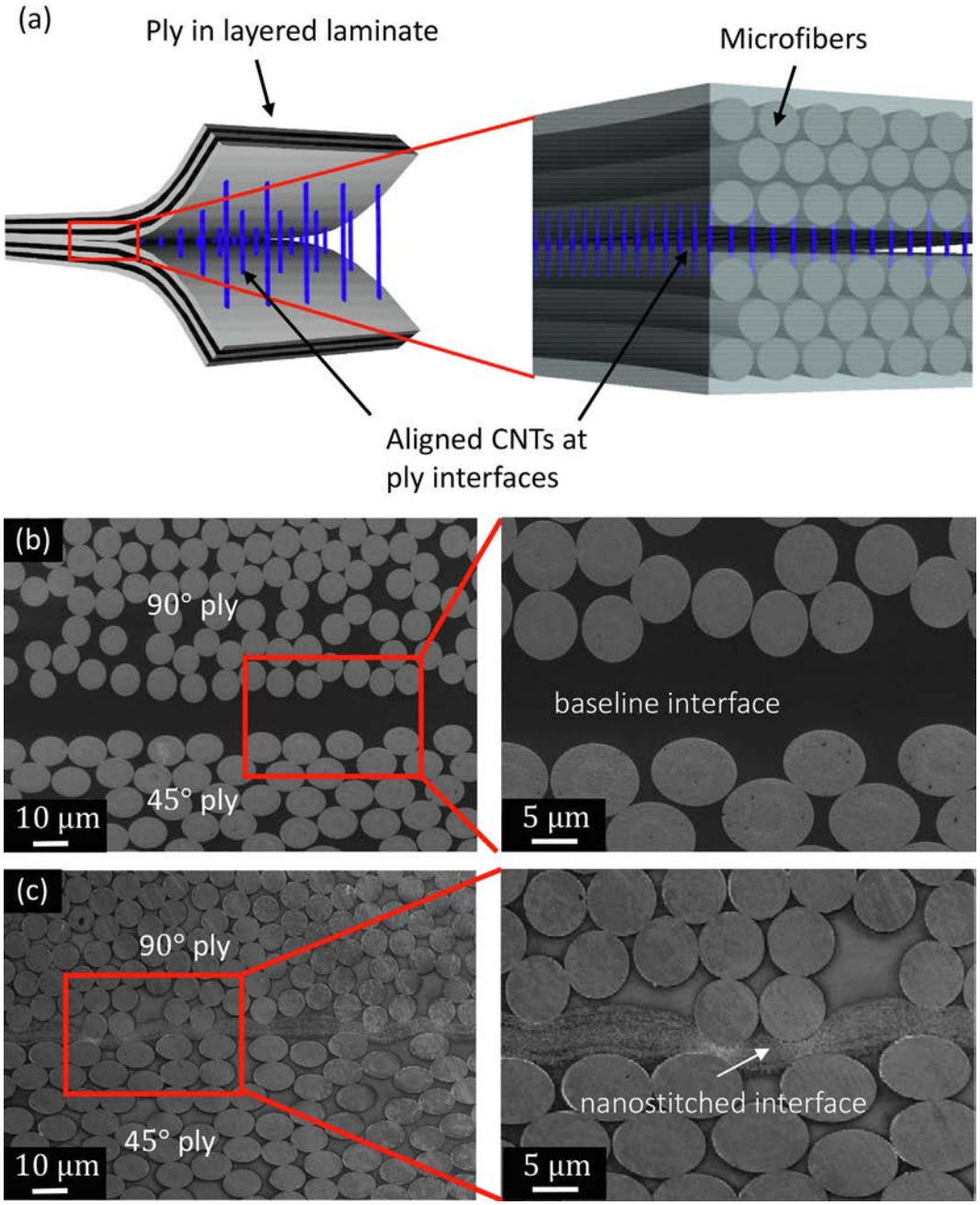

Fig. 1. Hierarchical nano-engineered composite architecture showing the placement of A-CNTs at the interface of the microfiber plies: (a) concept illustration of A-CNTs at a nanostitched laminate interface. Representative scanning electron micrographs (SEMs) of: (b) 90/45 interface of a baseline and (c) A-CNT reinforced sample showing the A-CNTs filling the interlaminar region with some bridging of the first layer of microfibers in both plies. Note the carbon microfibers are seen in cross sections in (b) and (c). (For interpretation of the references to colour in this figure legend, the reader is referred to the web version of this article.)

sonication [31–33]; however, all of these approaches are known or expected to induce damage to the CNTs, such as sonication-induced scission [34–36], which diminishes the efficacy of CNT reinforcement. Consequently, the improvements in fracture toughness, stiffness, and strength reported in the literature have been largely inconsistent and/or nonexistent [31,37,38].

Apart from mixing CNTs into (generally epoxy) resins and performing wet layup or infusion, deposition of CNTs via electrophoresis [39] or chemical vapor deposition (CVD) [40–44] on microfibers is another route that allows hierarchical composites to be realized without damaging the microfibers, for later infusion or wet layup processing. Garcia et al. [18] introduced a hierarchical architecture (now termed “nanostitch”) to allow a hierarchical composite to be created utilizing aligned CNTs (A-CNTs) and prepreg-based processing, including the industrially-relevant unidirectional (UD) fiber prepregs (vs. woven) that broadly provide the highest structural performance. A-CNTs were introduced into the interlaminar region between plies of UD composite prepreg that act as nanoscale stitches (see Fig. 1). The A-CNTs provide through-thickness reinforcement in the interlaminar region without the drawbacks that are normally associated with z-pining and stitching. This approach also allows resin to infiltrate between CNTs through capillary forces due to the vertical alignment of the CNTs, and thus provides the potential for higher CNT loading (>1%) [45–47]. As a result of the higher volume fraction and vertical alignment of CNTs, it has been demonstrated that these nanostitched laminates have both improved interlaminar fracture toughness [18,48] (2.5–3×

enhancement of mode I and mode II fracture toughness) and 14–40% increase in substructural in-plane strengths, [49] thus accomplishing increased interlaminar and intralaminar laminate-level properties. However, fatigue behavior for this type of nano-engineered prepreg composite architecture has not been reported, although related studies using woven plies and wet layup processing provide some comparison and useful results to guide this work. One notable difference with woven vs. UD systems is the relative size (~100 μm vs. ~10 μm, respectively) of the interlaminar region thickness, allowing process-zone toughening in the former that is not available for the UD composites. In the limited extant work, the reported change in fatigue performance has been inconsistent and the mechanisms for the improvement still remain unclear. Fenner et al. [50] reported an order of magnitude increase in shear fatigue life for a woven carbon fiber composite with the polymer matrix reinforced with CNTs and attributed the improvement in fatigue to CNTs blunting or re-directing the advancing crack. Similarly, Ladani et al. [51] reported large increases in mode I fracture due to both CNT reinforcement of the matrix and synergistic enhancement when combined with traditional z-pinning. Grimmer et al. [52] found that incorporating CNTs in the matrix of glass fiber reinforced plastics (GFRPs) slowed the crack propagation by CNT bridging, fracture, and pullout with a 2–3× improvement in mode I fatigue life. Borrego et al. [53], however, reported a 10% decrease in fatigue strength at 10^6 cycles for similar GFRP woven laminates, which was attributed to the formation of CNT agglomerates. In all of the extant work, comparisons of the size and morphology of the interlaminar region are unreported. Here, the effects of nanostitching on the static and fatigue response of nanostitched aerospace-grade CFRP UD prepreg composites via short-beam shear (SBS) tests are explored, supplemented by static progressive damage models, to better understand the strengthening and toughening mechanisms at the nano- and micro-scale originating from such a hierarchical architecture, with careful attention to characterizing the interlaminar region (see Fig. 1) both with and without CNT reinforcement.

2. Methods

Fabrication of the composite laminates is first presented, including A-CNT synthesis, A-CNT transfer to the prepreg plies, and laminate fabrication and characterization, followed by the detailed experimental procedure of static and fatigue SBS testing. A numerical damage progression model to simulate both interlaminar and intralaminar damage in the laminates is also presented.

2.1. A-CNT synthesis, laminate fabrication, and characterization

The A-CNTs were grown in a 44 mm inner diameter quartz tube furnace (Lindberg/BlueM) by chemical vapor deposition (CVD) on 3 cm × 4 cm Si substrates, and exhibit an average outer diameter of ~8 nm (3–7 walls with an inner diameter of ~5 nm and intrinsic CNT density of ~1.6 g/cm^3), inter-CNT spacing of ~60 nm, and volume fraction of ~1% CNTs [54–56]. The growth time was set to be 55 s to produce ~20 μm tall forests. At the end of each growth cycle, water was introduced in the tube for 45 s to reduce the attachment between the CNTs and the Si substrate and facilitate the transfer of the CNTs [49,54,57]. The height of the CNTs were obtained by measuring the z-axis travel between focal planes (Si substrate to top of the forest) on an optical microscope in dark field mode [58]. Three points (two near the substrate edge and one at the center) on the centerline across the wafer width (3 cm) direction were measured. The forest height is taken as the average of the three measurements. This method has a resolution of ±2 μm and the accepted average measured height of the A-CNTs ranges from 15 μm to 25 μm. The A-CNT forests were introduced to the interlaminar region between aerospace-grade UD AS4/8552 (Hexel) prepreg by manually transferring them onto the surface of the prepreg following already-reported procedures [45,59,60]. First, the Si substrate was positioned with the CNT side in contact with the prepreg ply surface, and then the Si substrate/ply assembly was placed on a hot plate at 60 °C for 30 s in order to increase the tackiness of the 8552 epoxy matrix to improve A-CNT transfer effectiveness, while gentle pressure was applied. After this step, the A-CNTs are adhered to the ply surface so that the Si substrate can be removed and the next ply can be laid up. This A-CNT transfer process was repeated for each interface during the layup process until the entire stacking sequence was complete. It is worth noting that the alignment of the A-CNT forests is preserved after transfer as seen in Fig. S1 (in Supplementary Materials), consistent with prior observations [61]. The prepreg is designed to yield a 63.5% microfiber volume fraction, and nominal per-ply thickness of 0.130 mm. A 16-ply quasi-isotropic layup ($[(0/90/\pm45)_2]_s$) having all 15 interfaces reinforced with A-CNTs creates the "nanostitched laminate", and it is noted that A-CNT transfer was over 95% effective based on surface area. Baseline laminates are manufactured in the same way apart from the A-CNT reinforcement. The laminates were cured in an autoclave following the manufacturer specifications: 6 bar of total pressure at 1–3 °C/min to 110 °C, hold for 1 h, heat again at 1–3 °C/min to 180 °C, hold for 2 h, cool down at 3–5 °C/min to 60 °C and vent pressure, let cool to room temperature. Once the laminates were cured, the edges were trimmed and specimens were cut and polished to size following ASTM D2344 [62]. Representative scanning electron microscopy (SEM) images in Fig. 1 show that the A-CNTs interpenetrate the adjacent plies and generally fill the resin-rich regions between them. The thickness of all specimens, baseline and nanostitched, were measured. Baseline laminates have thickness of 2.05 ± 0.02 mm and nanostitched laminates have thickness of 2.07 ± 0.01 mm, indicating that nanostitching does not measurably increase the interlaminar thickness, consistent with other work following the same procedures [49], thereby retaining the overall laminate microfiber volume fraction and other attributes.

2.2. Static SBS testing

Following ASTM D2344 [62] for the dimensions of the SBS coupon: (a) the width w of the coupon should be twice its thickness t, (b) the length l of the coupon should be 6× its thickness t, and (c) the span length s should be 4× its thickness. Following the Standard, the specimens were first cut with a diamond saw and then further polished in the following order: 500 grit sandpaper, 800 grit sandpaper, and 1 μm Al_2O_3 suspension to meet the desired dimension specifications (2 mm thick, 4 mm wide and 12 mm long). The polished specimens were then subjected to a 3-point bending load (6 mm diameter for loading nose and 3 mm diameter for supports) with an 8 mm span (See Fig. 2a). The test was performed on Zwick/Roell Z010 with a 10 kN load cell in displacement control. Following the standard, each specimen was loaded at 1 mm/min until one of the following occurred: (a) a load drop-off of 30%, (b) two-piece specimen failure, or (c) the head travel exceeded the specimen nominal thickness. Load and displacement were recorded every 250 ms, and the static SBS strength was calculated as:

$$\sigma_{SBS} = 0.75 \times \frac{F_{max}}{wt} \tag{1}$$

where σ_{SBS} is the SBS strength, and F_{max} is the maximum load. This value is a closed-form approximation of the maximum shear based on classical beam theory [63].

2.3. Fatigue SBS testing

Although not an ASTM or ISO Standard, several groups [64–68] have utilized the SBS configuration for fatigue testing, which principally adopts the ASTM D2344 Standard but for fatigue. Thus, the test configuration for fatigue is the same as shown in Fig. 2a, except that we replaced monotonic loading with a cyclic sinusoidal stress-controlled loading. Testing was performed using an Instron fatigue system (model 1332). The specimens were loaded at stress amplitudes that are 90%,

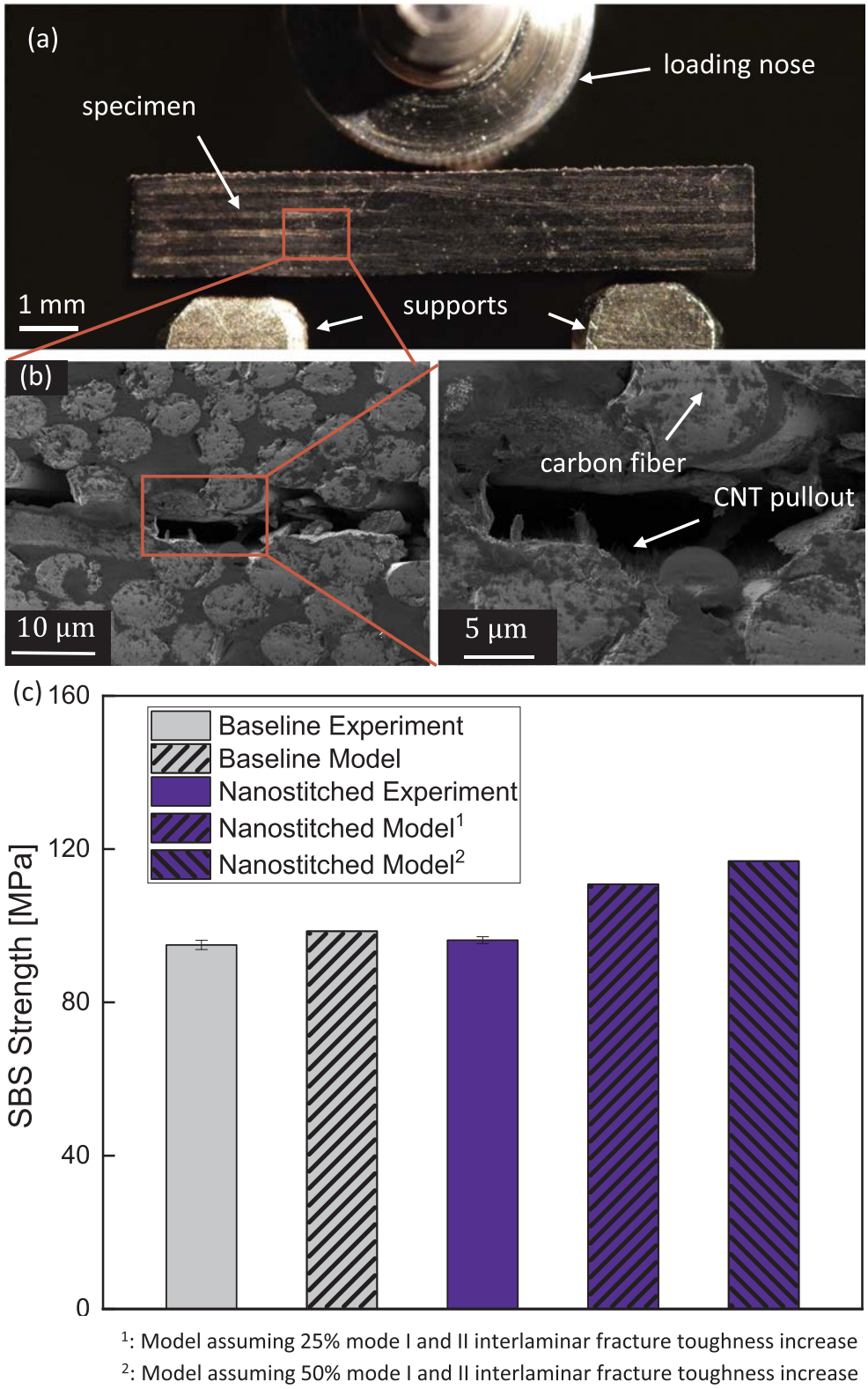

Fig. 2. Results of static SBS testing: (a) SBS test configuration (with A-CNT reinforced at every interface), (b) scanning electron micrographs of a broken A-CNT reinforced interface showing multi-micron-long CNTs pulled out of the polymer matrix, (c) SBS test results compared with numerical results from damage progression prediction model with two assumptions (25% and 50% mode I and II interlaminar fracture toughness improvement due to nanostitch). (For interpretation of the references to colour in this figure legend, the reader is referred to the web version of this article.)

80%, 70%, and 60% of the static SBS strength of the baseline. The frequency of the applied stress was 10 Hz. Tests were stopped and the specimen considered failed under two conditions: (a) when the specimen failed catastrophically, or (b) when the maximum displacement in a load cycle, as measured from the test machine cross-head, had changed by more than 20%, indicating a significant damage event [64]. The failure cycle was recorded for each load level and was used to produce the classical stress vs. life cycles curve (S-N curve) in Fig. 4.

Post-mortem specimens were scanned using the Nikon Metrology (X-Tek) HMXST225 Micro-CT system at the Center for Nanoscale Systems at Harvard University, and the Zeiss Xradia 520 Versa at the Institute for Soldier Nanotechnologies at Massachusetts Institute of Technology.

2.4. Damage progression prediction model

A finite element model was developed to better understand the effects of nanostitching on the SBS strength. The model used two separate constitutive models to simulate laminate damage: for intralaminar damage, a continuum model first developed by Maimí et al. [69,70] was used. This model uses a set of scalar damage variables to represent the failure mechanisms occurring in the longitudinal and transverse directions of a ply. Damage activation functions are based on the LaRC04 failure criteria [71]. For interlaminar damage, a cohesive zone model (CZM) [72,73] was implemented in ABAQUS [74] that relates closing traction τ to the crack opening displacement δ, with the energy dissipated per unit area to advance the crack taken from the area under the $\tau - \delta$ curve. The effect of A-CNTs on the interlaminar fracture toughness was modeled by increasing the mode I and mode II interlaminar fracture toughness, represented simply as Γ, by the same amount. The engineering solutions proposed by Turon et al. [75,76] were used to calculate the cohesive stresses. Details of both constitutive models can be found elsewhere [69,70,74,77]. In order to isolate the effect of interlaminar fracture toughness enhancement on SBS strength, all of the parameters in the model were kept constant, between the baseline and nanostitched specimens, except for the mode I and mode II interlaminar fracture toughness. The interlaminar fracture toughness (both mode I and mode II) was commonly scaled from 1–5× of the baseline, and the specimen response including SBS strength was computed as a function of the toughness scaling. The 1–5× enhancement range used in simulation was based on previous related work [18], where the authors experimentally measured a 2.5–3× enhancement mode I and II fracture toughness enhancement due to the introduction of A-CNTs. However, the authors used a slightly different manufacturing technique, therefore in this study we adopted a wider range of enhancement ratio simply as a reasonable estimate about 3×. Due to the lack of existing measured properties for the AS4/8552 material system, we followed prior work [78] and used the known values of a very similar material system, IM7/8552 [79–81]. Detailed inputs to the model can be found in the work by Furtado et al. [77].

3. Results and discussion

The static and fatigue results are discussed, including finite element analysis of progressive damage accumulation in the static SBS configuration.

3.1. Experiment and modeling results for static SBS strength

All tested specimens failed in a brittle manner via the load criterion (a load drop of 30%), rather than 2-piece specimen failure or the deflection criteria (see Section 2.2). Representative force–displacement curves can be found in Fig. S2 (in Supplementary Materials). Fig. 2c shows that there is no statistically significant difference between baseline and nanostitched specimens for static SBS strength. The baseline specimens were found to have an SBS strength of 95.0 ± 1.2 MPa, whereas the nanostitched specimens were found to have an SBS strength of 96.2 ± 0.9 MPa. The baseline SBS strength is 15% higher than the 82.3 ± 4.7 MPa reported by the National Institute for Aviation Research (NIAR) [82]. However, a different layup ([(45/0/-45/90)$_{3s}$]) was used in the prior work by NIAR, and composite layup has been shown to affect the stress distribution inside an SBS specimen [72,73,83,84]. The lack of SBS strength increase is different from previous results of Lewis et al. [60] for a very similar UD material system (IM7/8552) and the same layup that showed a >8% statistically significant static SBS strength increase. Representative micrographs across different length scales are shown in Fig. 2b, where CNT pullout is clearly evident. As has been noted by others, the stress distribution in a laminated composite under SBS loading is complex [63,83]. Composite layup, fiber/matrix material type, specimen geometry, manufacturing defects, etc. have all been shown to affect the ultimate SBS strength. Previous studies [84–86] have shown large departures from the classical beam solution when utilizing higher order elastic analyses. In particular, large compressive stresses also exist in the same region where the shear stress concentrates, having the effect of suppressing interlaminar shear failure. It has been suggested by many [84,87] that the SBS test best serves as a useful screening and comparative test. Valid SBS tests are used to explore interface strength and toughening in static testing on a comparative basis [87], and some (see discussion in next section) have utilized the SBS test for fatigue as well. In relation to the current work where a tougher and stronger interface due to A-CNT reinforcement appears to exist (see fatigue data in next section), it is possible that the strength increase will (i) be below the statistical threshold for improvement, or (ii) be masked in the SBS test due to more complex (and coupled) failure mechanisms. Therefore, even if a stronger and tougher interface due to A-CNT reinforcement exists, the ultimate failure load may still be dictated by other more complex (and likely coupled) failure mechanisms.

In order to further understand the experimental results, particularly the finding that SBS static strength is not enhanced by nanostitching, a sensitivity analysis of the SBS strength as a function of interlaminar fracture toughness Γ enhancement ratio ($\Gamma_{nanostitched}/\Gamma_{baseline}$) was performed using the finite element method, as described in Section 2.4. The validity of the model was first verified by comparing the simulation results for SBS strength to our baseline experiments (see Fig. 2c). The simulation results showed good agreement with the experiment with an error less than 4% for the predicted SBS strength. Fig. 3a shows the numerical results for SBS strength vs. the enhancement ratio of fracture toughness. It was found that for AS4/8552 prepreg laminates, the SBS strength does not increase proportionally to the increase of fracture toughness. A plateau in SBS strength at +50% can be clearly seen after the toughness enhancement reaches ~3× of the baseline. Here, a 5% increase in both mode I and mode II fracture toughness results in a ~4% increase in SBS strength, whereas a 15% increase in fracture toughness results in only a ~6% improvement in SBS strength. Increases in strength of this magnitude are undetectable in the probabilistic SBS strength data with standard errors on this order. This relative insensitivity of static SBS strength to the interlaminar fracture toughness suggests that other damage mechanisms, such as intralaminar damage, play a significant role in determining the SBS strength, as discussed above. The model can also predict and visualize damage progression at various load points via scalar damage variables. Fig. 3b shows load–displacement curves for mode I and II toughness enhancement $\Gamma_{nanostitched}/\Gamma_{baseline}$ = 100%, 200%, and 500%, respectively, where point A is at the maximum load and point B is 50% of the maximum load after the load drop, and Fig. 3c shows the damage at these two points. As can be seen from these figures, there is no noticeable change of damage modes even when the interlaminar fracture toughness enhancement is twice as large as that of the baseline, *i.e.*, both failures are dominated by interlaminar damage. Furthermore, it would require at least 5× enhancement of fracture toughness to shift the damage modes from predominantly interlaminar damage to predominantly intralaminar damage. The simulation results are consistent with our hypothesis in the first paragraph of this Section that the enhancement in the fracture toughness of the interface results in undetectable improvement in static SBS strength due to complex (and coupled) failure mechanisms. By contrast, the next section will show that in the fatigue tests, a damage mode shift from interlaminar to intralaminar in fatigue is observed (along with a significant increase in fatigue life).

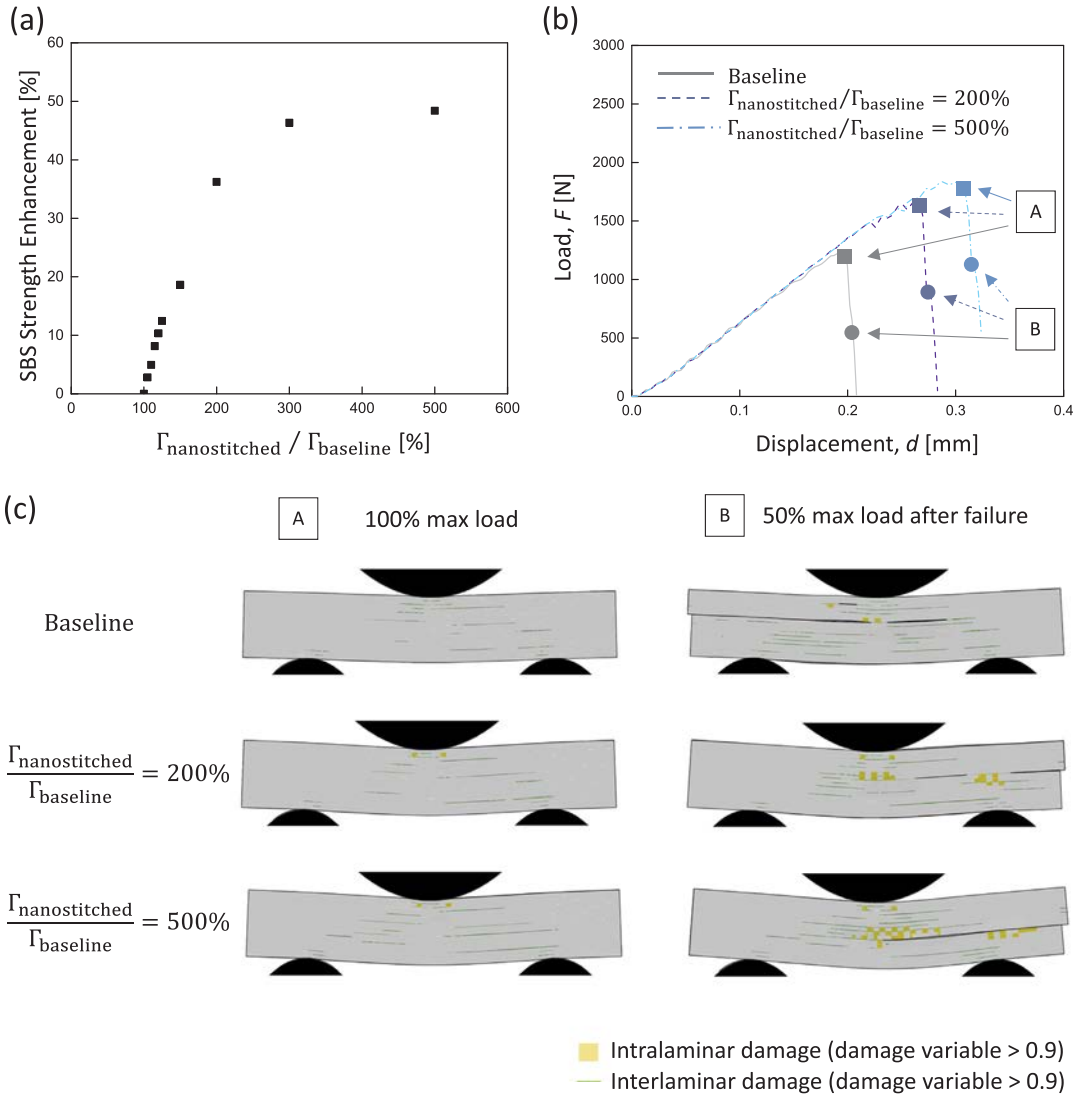

Fig. 3. Finite element damage progression simulation results: (a) representative load-deformation curve in SBS for interlaminar fracture toughness enhancement ratio of 100% (baseline), 200%, and 500%. Points A and B are at 100% and 50% of the maximum load, respectively, (b) static SBS strength as a function of interlaminar fracture toughness enhancement ratio, and (c) representation of damage at points A and B in (a). Damage is represented by a set of scalar variables, which can take values from 0 (*i.e.*, no damage) to 1 (*i.e.*, completely damaged crack) and are colored when their associated damage variables are greater than 0.9. (For interpretation of the references to colour in this figure legend, the reader is referred to the web version of this article.)

3.2. Testing results for fatigue SBS strength

On average across the load levels tested (60%, 70%, 80%, and 90% of SBS static strength), the fatigue life increased by 115%. Detailed values for fatigue life are provided in Table S1. Fig. 4a shows the lifetime of the specimens plotted against the stress amplitude. Statistically significant fatigue life enhancement was observed at each load level. The majority (80%) of fatigue specimens failed catastrophically, indicating a sudden damage event with no prior indication (audibly or via maximum displacement increase) of pre-ultimate damage, *i.e.*, the specimens failed in a brittle manner, whereas the minority (20%) failed via the maximum displacement increase criterion. The minority (20%) of specimens that failed via the maximum displacement increase criterion were distributed across the test matrix with no trend observed (*e.g.*, high-cycle vs. low-cycle fatigue). The failure modes observed in this work are different from the results of May et al. [64] where a 20-ply UD IM7/8552 layup was used and the majority of the fatigue specimens failed via the displacement increase criterion at lower load levels. The difference in the failure modes could be mainly attributed to the different layups of the two tests. May et al. [64] adopted a UD layup where fiber nesting was very likely to be present, *i.e.*, no clear interfaces existed between adjacent plies, which allowed the crack to easily propagate into the intralaminar region. As a macroscopic consequence, the specimens did not fail in a brittle manner. Representative effective compliance curves to indicate damage [64] are plotted against the number of cycles as shown in Fig. S3 (in Supplementary Materials). There was almost no change in compliance during the first 99% of the fatigue life, and a fast and significant increase of the compliance very close to failure. A similar observation was also reported by Makeev et al. [83]. The lack of compliance change over time is in agreement with the brittle failure manner of the majority of the specimens. In order to understand the mechanism of lifetime increase due to the A-CNT reinforcement, two *post-mortem* specimens that were loaded at 70% of the static SBS strength (*i.e.*, 66.5 MPa), but did not fail catastrophically, were scanned using micro-computed tomography (micro-CT). Micro-CT provides a non-destructive way to examine the internal 3D damage states of the samples, [88] and it was not until very recently that micro-CT techniques have been used in fatigue studies of polymer matrix composites (without nano-scale reinforcement) [89]. Fig. 4b shows a slice of the cross-section of the two specimens and highlights a

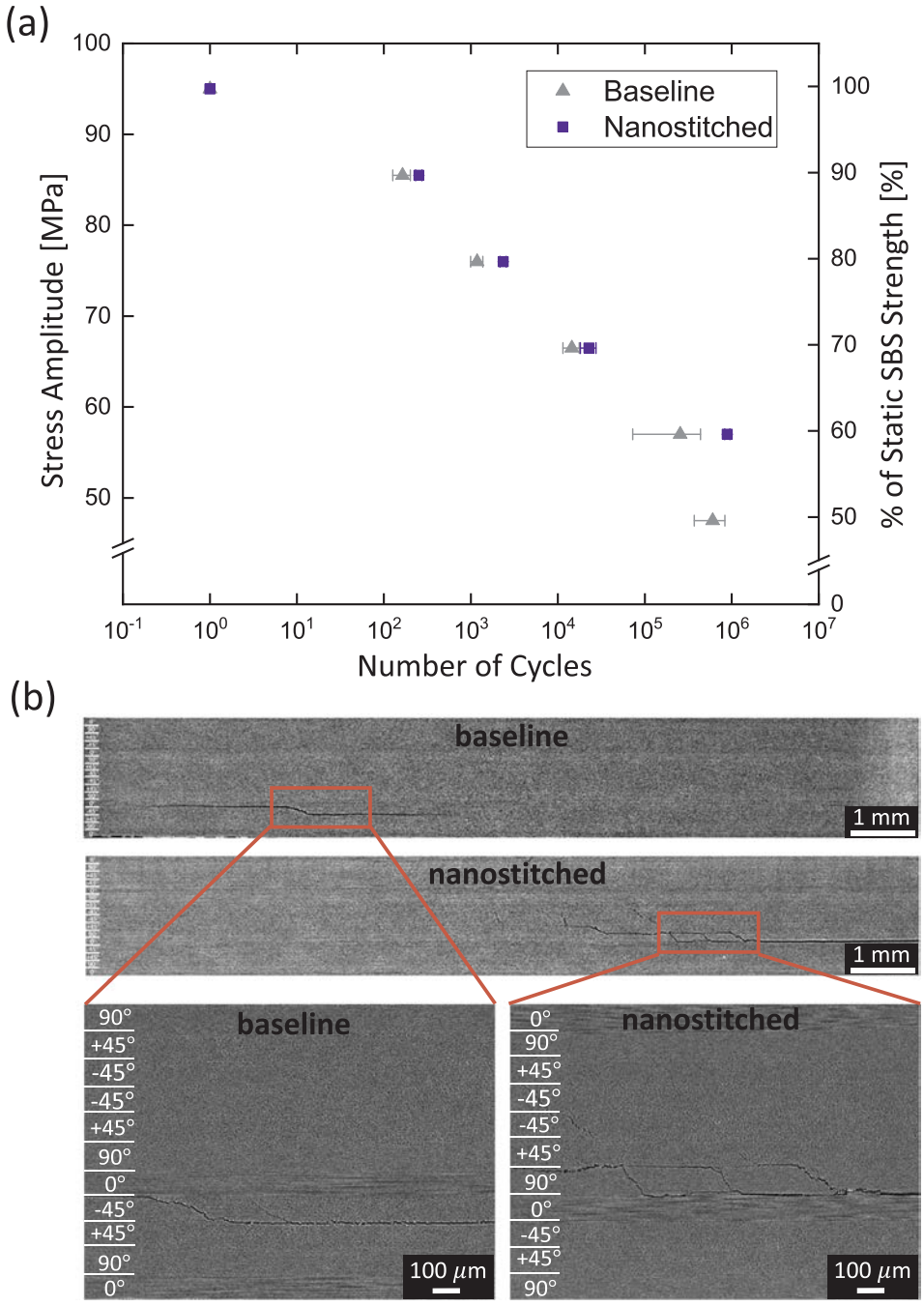

Fig. 4. Fatigue test results: (a) S-N curve showing a 3× improvement at lower stress levels (high-cycle fatigue), and (b) micro-computed tomography (micro-CT) images of *post-mortem* baseline and "nanostitched" specimens at 70% of the static SBS strength that failed via the displacement criteria, where the nanostitched specimen indicates significant intralaminar damage at multiple plies. Ply interfaces and orientations are annotated in all images. (For interpretation of the references to colour in this figure legend, the reader is referred to the web version of this article.)

major difference in the damage accumulation between baseline and A-CNT reinforced specimens. In the baseline failed specimen, long, straight, and clean interlaminar cracks are clearly visible. In contrast, the nanostitched specimen exhibits a much more diffusive crack pattern, with extensive intralaminar matrix cracking in addition to smaller interlaminar cracks. The diffusive crack pattern suggests that the nanostitched specimen has a tougher and stronger interface so that it delays delamination and shifts some of the damage from the interlaminar region to the intralaminar region. Similar observations have been noted in the IM7/8552 work discussed previously where SBS static shear strength increased [60]. It is worth noting that there is a 249% increase in the specimen lifetime when the load is 60% of the static SBS strength, *i.e.*, in the high-cycle fatigue regime. This shows that for this material system, A-CNTs are especially effective in suppressing damage in high-cycle fatigue situations, an important loading condition in aerospace applications. To further explore the effect of nanostitch on high-cycle fatigue, four additional baseline specimens were tested under 50% of the static SBS strength, and they failed at ~0.60 ± 0.23 million cycles, in comparison to the nanostitched specimens that failed at ~0.89 ± 0.06 million cycles under 60% of the static SBS strength. In other words, the nanostitched specimens were able to last ~1 million cycles under at least 20% higher load than the baseline specimens. The detailed fatigue life is provided in Table S1 (in Supplementary Materials). Grimmer et al. [52,90] reported the same trend of

improvement of their CNT-reinforced hybrid woven epoxy composites, *i.e.*, more effectiveness of CNTs at low stress levels relative to high stress levels. They suggested that at high stress levels, the CNTs shift from high-energy dissipating pull-out behavior to a relatively low-energy dissipating fracture behavior, in line with observations of varying volumes of pulled-out CNTs in the different regimes. Bortz et al. [91] observed similar fatigue behavior of their carbon nanofiber (CNF) epoxy nanocomposite. They concluded that at low applied stress levels, the CNF/matrix bond is strong enough to transfer the localized stresses from the weaker matrix to CNFs in the form of small-scale straining. This redistribution of the stresses slows the rate of fatigue crack propagation. At higher stress levels, the localized stresses are high enough to break the CNF/matrix interface. Those authors also identified large increases in fatigue life due to the presence of CNFs, yet effectively no increase in static toughness - the same behavior as observed here in the nanostitched hierarchical composite. Further work in high-cycle fatigue is warranted, as is more detailed analysis of the damage states of specimens pre-ultimate failure at different fatigue stress intensity levels.

4. Conclusions

A hierarchical composite architecture was realized by integrating A-CNTs at ply interfaces of aerospace-grade carbon microfiber UD prepreg advanced composites. The transfer of A-CNTs can be readily implemented in existing laminate manufacturing without damaging or disturbing in-plane microfibers, and no increase in the laminate thickness is observed when integrating the ~20 μm A-CNTs at all ply interfaces, consistent with prior work [49]. The SBS fatigue test showed increases in fatigue life on average and across all load levels (60–90% of static SBS strength), with a larger (249%) improvement observed for high-cycle fatigue (60% of static SBS strength). Micro-CT scans of *post-mortem* fatigue specimens suggest a distinct difference in fatigue damage mechanism: A-CNTs seem to suppress delamination and shift the damage to the intralaminar region. No static SBS strength improvement was observed, which is attributed to the complex stress state and failure modes in SBS, and the relative insensitivity of SBS strength to the interlaminar fracture toughness enhancement (*e.g.*, a 50% increase in interlaminar toughness yielding an SBS strength increase of less than 20% in progressive damage simulations). Furthermore, the model suggests that a 5× increase in fracture toughness is needed to alter the damage modes in static SBS tests. The extant literature has mixed findings with regard to fatigue behavior of CNT-reinforced laminates, likely due to differences in processing, materials, and uncharacterized CNT and interface morphology, typical of woven systems and wet layup processing. By contrast, the system studied herein utilizes prepreg processing which is highly repeatable (one of its clear industrial advantages) and the interface is very well characterized: the CNTs are 20 μm in height and at 1 vol%, span the interlaminar region with no voids and interdigitate across microfibers less than one microfiber diameter. Such morphologically-controlled systems allow for repeatability and greater insight as modeling can be reasonably undertaken as demonstrated here. The results presented here lead to clear next steps. First, further work in high-cycle fatigue loading is warranted. The damage states of specimens that have not failed, but experienced high-cycle fatigue, should be analyzed in a broadened micro-CT campaign, employing *in situ* techniques if available. Second, the effect of higher A-CNT loading (>1%) on laminate strength and toughness, potentially achievable via densifying as-grown A-CNT forests, *e.g.,* mechanical [44] or capillary densification [92], should be studied. Third, the actual enhancement of mode I and II fracture toughness due to the introduction of A-CNTs should be evaluated experimentally, followed by the development of cohesive zone models (CZMs) that take into account inelastic deformation, fracture of the A-CNT reinforced interfaces, and the shape change of the cohesive law. Once this information becomes available, hierarchical composites with enhanced strength, fracture toughness, and fatigue life may be rationally designed and manufactured, which could enable the realization of aerospace composite structures with extended service life.

Acknowledgements

This work was supported by the U.S Office of Naval Research under grant/contract number N00014-13-1-0213, by Airbus, Embraer, Lockheed Martin, Saab AB, Hexcel, Saertex, TohoTenax, and ANSYS through MIT's Nano-Engineered Composite aerospace STructures (NECST) Consortium, and through the Defense University Research Instrumentation Program (DURIP) under grant number ONR. N000141712068 for micro-computed tomography instrumentation support. This work was partially funded by National Funds through FCT - Fundação para Ciência e a Tecnologia in the scope of project MITP-TB/PFM/0005/2013. This work made use of facilities supported in part by the U.S. Army Research Laboratory and the U. S. Army Research Office through the Institute for Soldier Nanotechnologies, under contract number W911NF-13-D-0001, by the U.S. Army Natick Soldier R, D & E Center (NSRDEC), and carried out in part through the use of MIT's Microsystems Technology Laboratories. This work was performed (in part) at the Center for Nanoscale Systems (CNS), a member of the National Nanotechnology Infrastructure Network (NNIN), which is supported by the National Science Foundation under NSF award No. ECS-0335765. CNS is part of Harvard University. The authors thank Saab AB for materials (prepreg) donation. The second author would like to thank Fundação para a Ciência e a Tecnologia (FCT), grant SFRH/BD/115859/2016. The authors thank Dr. Itai Stein, Reed Kopp, Nathan Fritz, Ashley Kaiser, Jeonyoon Lee, and the entire necstlab at MIT for their valuable discussion and input.

Appendix A. Supplementary material

Supplementary data associated with this article can be found, in the online version, at https://doi.org/10.1016/j.compositesa.2019.02.023.

References

[1] Faggiani A, Falzon B. Predicting low-velocity impact damage on a stiffened composite panel. Compos Part A-Appl S 2010;41(6):737–49. https://doi.org/10.1016/j.compositesa.2010.02.005.
[2] Tong L, Mouritz AP, Bannister MK. 3D fibre reinforced polymer composites. 1st ed. Elsevier Science; 2002.
[3] Dransfield KA, Jain LK, Mai Y-W. On the effects of stitching in CFRPs-I. Mode I delamination toughness. Compos Sci Technol 1998;58(6):815–27. https://doi.org/10.1016/S0266-3538(97)00229-7.
[4] Mouritz A, Leong K, Herszberg I. A review of the effect of stitching on the in-plane mechanical properties of fibre-reinforced polymer composites. Compos Part A-Appl S 1997;28(12):979–91. https://doi.org/10.1016/S1359-835X(97)00057-2.
[5] Larsson F. Damage tolerance of a stitched carbon/epoxy laminate. Compos Part A-Appl S 1997;28(11):923–34. https://doi.org/10.1016/S1359-835X(97)00063-8.
[6] Partridge IK, Cartié DD. Delamination resistant laminates by Z-Fiber® pinning: Part I manufacture and fracture performance. Compos Part A-Appl S 2005;36(1):55–64. https://doi.org/10.1016/j.compositesa.2004.06.029.
[7] Tan K, Yoshimura A, Watanabe N, Iwahori Y, Ishikawa T. Effect of stitch density and stitch thread thickness on damage progression and failure characteristics of stitched composites under out-of-plane loading. Compos Sci Technol 2013;74:194–204. https://doi.org/10.1016/j.compscitech.2012.11.001.
[8] Aymerich F. Effect of stitching on the static and fatigue performance of co-cured composite single-lap joints. J Compos Mater 2004;38(3):243–57. https://doi.org/10.1177/0021998304039271.
[9] Siddiqui NA, Woo RS, Kim J-K, Leung CC, Munir A. Mode I interlaminar fracture behavior and mechanical properties of CFRPs with Nanoclay-filled epoxy matrix. Compos Part A-Appl S 2007;38(2):449–60. https://doi.org/10.1016/j.compositesa.2006.03.001.
[10] Yokozeki T, Iwahori Y, Ishiwata S, Enomoto K. Mechanical properties of CFRP laminates manufactured from unidirectional prepregs using CSCNT-dispersed epoxy. Compos Part A-Appl S 2007;38(10):2121–30. https://doi.org/10.1016/j.compositesa.2007.07.002.
[11] Fiedler B, Gojny FH, Wichmann MH, Nolte MC, Schulte K. Fundamental aspects of nano-reinforced composites. Compos Sci Technol 2006;66(16):3115–25. https://doi.org/10.1016/j.compscitech.2005.01.014.
[12] Sager R, Klein P, Lagoudas D, Zhang Q, Liu J, Dai L, et al. Effect of carbon nanotubes on the interfacial shear strength of T650 carbon fiber in an epoxy matrix. Compos Sci Technol 2009;69(7-8):898–904. https://doi.org/10.1016/j.compscitech.2008.

12.021.
[13] Thakre PR, Lagoudas DC, Riddick JC, Gates TS, Frankland S-JV, Ratcliffe JG, et al. Investigation of the effect of single wall carbon nanotubes on interlaminar fracture toughness of woven carbon fiber-epoxy composites. J Compos Mater 2011;45(10):1091–107. https://doi.org/10.1177/0021998310389088.
[14] Kumar SK, Benicewicz BC, Vaia RA, Winey KI. 50th Anniversary perspective: are polymer Nanocomposites practical for applications? Macromolecules 2017;50(3):714–31. https://doi.org/10.1021/acs.macromol.6b02330.
[15] Gorbatikh L, Wardle BL, Lomov SV. Hierarchical lightweight composite materials for structural applications. MRS Bull 2016;41(09):672–7. https://doi.org/10.1557/mrs.2016.170.
[16] De Volder MFL, Tawfick SH, Baughman RH, Hart AJ. Carbon nanotubes: present and future commercial applications. Science 2013;339(6119):535–9. https://doi.org/10.1126/science.1222453.
[17] Naskar AK, Keum JK, Boeman RG. Polymer matrix nanocomposites for automotive structural components. Nat Nanotechnol 2016;11(12):1026–30. https://doi.org/10.1038/nnano.2016.262.
[18] Garcia EJ, Wardle BL, John Hart A. Joining prepreg composite interfaces with aligned carbon nanotubes. Compos Part A-Appl S 2008;39(6):1065–70. https://doi.org/10.1016/j.compositesa.2008.03.011.
[19] Greenfeld I, Wagner HD. Nanocomposite toughness, strength and stiffness: role of filler geometry. Nanocomposites 2015;1(1):3–17. https://doi.org/10.1179/2055033214Y.0000000002.
[20] Eichhorn SJ, Dufresne A, Aranguren M, Marcovich NE, Capadona JR, Rowan SJ, et al. Review: current international research into cellulose nanofibres and nanocomposites. J Mater Sci 2010;45(1):1–33. https://doi.org/10.1007/s10853-009-3874-0.
[21] Che J, Çagin T, Goddard WA. Thermal conductivity of carbon nanotubes. Nanotechnology 2000;11(2):65–9. https://doi.org/10.1088/0957-4484/11/2/305.
[22] Berber S, Kwon Y-K, Tománek D. Unusually high thermal conductivity of carbon nanotubes. Phys Rev Lett 2000;84(20):4613–6. https://doi.org/10.1103/PhysRevLett.84.4613.
[23] Gojny F, Wichmann M, Fielder B, Schulte K. Influence of different carbon nanotubes on the mechanical properties of epoxy matrix composites – a comparative study. Compos Sci Technol 2005;65(15-16):2300–13. https://doi.org/10.1016/j.compscitech.2005.04.021.
[24] Dresselhaus MS, Dresselhaus G, Avouris P. Carbon nanotubes: synthesis, structure, properties, and applications. Springer; 2001.
[25] Marconnet AM, Panzer MA, Goodson KE. Thermal conduction phenomena in carbon nanotubes and related nanostructured materials. Rev Mod Phys 2013;85(3):1295–326. https://doi.org/10.1103/RevModPhys.85.1295.
[26] Meunier V, Souza Filho AG, Barros EB, Dresselhaus MS. Physical properties of low-dimensional sp2-based carbon nanostructures. Rev Mod Phys 2016;88(2):1–50. https://doi.org/10.1103/RevModPhys.88.025005.
[27] Ebbesen TW, Lezec HJ, Hiura H, Bennett JW, Ghaemi HF, Thio T. Electrical conductivity of individual carbon nanotubes. Nature 1996;382(6586):54–6. https://doi.org/10.1038/382054a0.
[28] Coleman JN, Khan U, Blau WJ, Gun'ko YK. Small but strong: a review of the mechanical properties of carbon nanotube–polymer composites. Carbon 2006;44(9):1624–52. https://doi.org/10.1016/j.carbon.2006.02.038.
[29] Gibson RF. A review of recent research on mechanics of multifunctional composite materials and structures. Compos Struct 2010;92(12):2793–810. https://doi.org/10.1016/j.compstruct.2010.05.003.
[30] Gao L, Chou T-W, Thostenson ET, Zhang Z, Coulaud M. In situ sensing of impact damage in epoxy/glass fiber composites using percolating carbon nanotube networks. Carbon 2011;49(10):3382–5. https://doi.org/10.1016/j.carbon.2011.04.003.
[31] Domun N, Hadavinia H, Zhang T, Sainsbury T, Liaghat GH, Vahid S. Improving the fracture toughness and the strength of epoxy using nanomaterials – a review of the current status. Nanoscale 2015;7(23):10294–329. https://doi.org/10.1039/C5NR01354B.
[32] Chandrasekaran V, Advani S, Santare M. Role of processing on interlaminar shear strength enhancement of epoxy/glass fiber/multi-walled carbon nanotube hybrid composites. Carbon 2010;48(13):3692–9. https://doi.org/10.1016/j.carbon.2010.06.010.
[33] Clancy AJ, Anthony DB, Fisher SJ, Leese HS, Roberts CS, Shaffer MSP, et al. Reductive dissolution of supergrowth carbon nanotubes for tougher nanocomposites by reactive coagulation spinning. Nanoscale 2017;9(25):8764–73. https://doi.org/10.1039/C7NR00734E.
[34] Amadei CA, Stein IY, Silverberg GJ, Wardle BL, Vecitis CD. Fabrication and morphology tuning of graphene oxide nanoscrolls. Nanoscale 2016;8(12):6783–91. https://doi.org/10.1039/C5NR07983G.
[35] Pagani G, Green MJ, Poulin P, Pasquali M. Competing mechanisms and scaling laws for carbon nanotube scission by ultrasonication. Proc Natl Acad Sci 2012;109(29):11599–604. https://doi.org/10.1073/pnas.1200013109.
[36] Stegen J. Mechanics of carbon nanotube scission under sonication. J Chem Phys 2014;140(24):244908. https://doi.org/10.1063/1.4884823.
[37] Arca MA, Coker D. Experimental investigation of CNT effect on curved beam strength and interlaminar fracture toughness of CFRP laminates. J Phys Conf Ser 2014;524:012038. https://doi.org/10.1088/1742-6596/524/1/012038.
[38] Lubineau G, Rahaman A. A review of strategies for improving the degradation properties of laminated continuous-fiber/epoxy composites with carbon-based nanoreinforcements. Carbon 2012;50(7):2377–95. https://doi.org/10.1016/j.carbon.2012.01.059.
[39] Sui X, Shi J, Yao H, Xu Z, Chen L, Li X, et al. Interfacial and fatigue-resistant synergetic enhancement of carbon fiber/epoxy hierarchical composites via an electrophoresis deposited carbon nanotube-toughened transition layer. Compos Part A-Appl S 2017;92:134–44. https://doi.org/10.1016/j.compositesa.2016.11.004.
[40] Wicks SS, de Villoria RG, Wardle BL. Interlaminar and intralaminar reinforcement of composite laminates with aligned carbon nanotubes. Compos Sci Technol 2010;70(1):20–8. https://doi.org/10.1016/j.compscitech.2009.09.001.
[41] Wicks SS, Wang W, Williams MR, Wardle BL. Multi-scale interlaminar fracture mechanisms in woven composite laminates reinforced with aligned carbon nanotubes. Compos Sci Technol 2014;100:128–35. https://doi.org/10.1016/j.compscitech.2014.06.003.
[42] Kundalwal S, Ray M. Effect of carbon nanotube waviness on the effective thermoelastic properties of a novel continuous fuzzy fiber reinforced composite. Compos Part B-Eng 2014;57:199–209. https://doi.org/10.1016/j.compositesb.2013.10.003.
[43] Thostenson ET, Li WZ, Wang DZ, Ren ZF, Chou TW. Carbon nanotube/carbon fiber hybrid multiscale composites. J Appl Phys 2002;91(9):6034–7. https://doi.org/10.1063/1.1466880.
[44] Yamamoto N, John Hart A, Garcia EJ, Wicks SS, Duong HM, Slocum AH, et al. High-yield growth and morphology control of aligned carbon nanotubes on ceramic fibers for multifunctional enhancement of structural composites. Carbon 2009;47(3):551–60. https://doi.org/10.1016/j.carbon.2008.10.030.
[45] Wardle BL, Saito DS, García EJ, Hart AJ, Guzman de Villoria R, Verploegen EA. Fabrication and characterization of ultrahigh-volume-fraction aligned carbon nanotube-polymer composites. Adv Mater 2008;20(14):2707–14. https://doi.org/10.1002/adma.200800295.
[46] Cebeci H, Guzman de Villoria R, Hart AJ, Wardle BL. Multifunctional properties of high volume fraction aligned carbon nanotube polymer composites with controlled morphology. Compos Sci Technol 2009;69(15-16):2649–56. https://doi.org/10.1016/j.compscitech.2009.08.006.
[47] Handlin D, Stein IY, Guzman de Villoria R, Cebeci H, Parsons EM, Socrate S, et al. Three-dimensional elastic constitutive relations of aligned carbon nanotube architectures. J Appl Phys 2013;114(22):224310. https://doi.org/10.1063/1.4842117.
[48] Falzon BG, Hawkins SC, Huynh CP, Radjef R, Brown C. An investigation of mode i and mode ii fracture toughness enhancement using aligned carbon nanotubes forests at the crack interface. Compos Struct 2013;106:65–73. https://doi.org/10.1016/j.compstruct.2013.05.051.
[49] Guzman de Villoria R, Hallander P, Ydrefors L, Nordin P, Wardle B. In-plane strength enhancement of laminated composites via aligned carbon nanotube interlaminar reinforcement. Compos Sci Technol 2016;133:33–9. https://doi.org/10.1016/j.compscitech.2016.07.006.
[50] Fenner JS, Daniel IM. Hybrid nanoreinforced carbon/epoxy composites for enhanced damage tolerance and fatigue life. Compos Part A-Appl S 2014;65:47–56. https://doi.org/10.1016/j.compositesa.2014.05.023.
[51] Ladani RB, Ravindran AR, Wu S, Pingkarawat K, Kinloch AJ, Mouritz AP, et al. Multi-scale toughening of fibre composites using carbon nanofibres and Z-pins. Compos Sci Technol 2016;131:98–109. https://doi.org/10.1016/j.compscitech.2016.06.005.
[52] Grimmer CS, Dharan C. Enhancement of delamination fatigue resistance in carbon nanotube reinforced glass fiber/polymer composites. Compos Sci Technol 2010;70(6):901–8. https://doi.org/10.1016/j.compscitech.2010.02.001.
[53] Borrego L, Costa J, Ferreira J, Silva H. Fatigue behaviour of glass fibre reinforced epoxy composites enhanced with nanoparticles. Compos Part B-Eng 2014;62:65–72. https://doi.org/10.1016/j.compositesb.2014.02.016.
[54] Lee J, Stein IY, Kessler SS, Wardle BL. Aligned carbon nanotube film enables thermally induced state transformations in layered polymeric materials. ACS Appl Mater Interfaces 2015;7(16):8900–5. https://doi.org/10.1021/acsami.5b01544.
[55] Liu K, Sun Y, Chen L, Feng C, Feng X, Jiang K, et al. Controlled growth of super-aligned carbon nanotube arrays for spinning continuous unidirectional sheets with tunable physical properties. Nano Lett 2008;8(2):700–5. https://doi.org/10.1021/nl0723073. arXiv:arXiv:1206.5023.
[56] Zhao B, Futaba DN, Yasuda S, Akoshima M, Yamada T, Hata K. Exploring advantages of diverse carbon nanotube forests with tailored structures synthesized by supergrowth from engineered catalysts. ACS Nano 2009;3(1):108–14. https://doi.org/10.1021/nn800648a.
[57] Lee J, Stein IY, Devoe ME, Lewis DJ, Lachman N, Kessler SS, et al. Impact of carbon nanotube length on electron transport in aligned carbon nanotube networks. Appl Phys Lett 2015;106(5):053110. https://doi.org/10.1063/1.4907608.
[58] Lewis DJ. Interlaminar reinforcement of carbon fiber composites from unidirectional prepreg utilizing aligned carbon nanotubes Master's thesis Cambridge, MA, USA: Massachusettes Insitutute of Technology; 2016.
[59] Hart AJ, Slocum AH. Rapid growth and flow-mediated nucleation of millimeter-scale aligned carbon nanotube structures from a thin-film catalyst. J Phys Chem B 2006;110(16):8250–7. https://doi.org/10.1021/jp055498b.
[60] Lewis D, Wardle BL. Interlaminar shear strength investigation of aligned carbon nanotube-reinforced prepreg composite interfaces. 56th AIAA/ASCE/AHS/ASC Struct. Struct. Dyn. Mater. Conf., No. January Reston, Virginia, USA: American Institute of Aeronautics and Astronautics; 2015. https://doi.org/10.2514/6.2015-0127.
[61] Kalfon-Cohen E, Kopp R, Furtado C, Ni X, Arteiro A, Borstnar G, et al. Synergetic effects of thin plies and aligned carbon nanotube interlaminar reinforcement in composite laminates. Compos Sci Technol 2018;166:160–8. https://doi.org/10.1016/j.compscitech.2018.01.007.
[62] ASTM. D2344/D2344M-16 standard test method for short-beam strength of polymer matrix composite materials and their laminates. West Conshohocken, PA: ASTM International; 2016. https://doi.org/10.1520/D2344_D2344M-16.
[63] Timoshenko S, Gere JM. Mechanics of materials. New York: Van Nostrand Reinhold Co; 1972.

[64] May M, Hallett SR. An assessment of through-thickness shear tests for initiation of fatigue failure. Compos Part A-Appl S 2010;41(11):1570–8. https://doi.org/10.1016/j.compositesa.2010.07.005.
[65] May M, Hallett S. Analysis of damage evolution in unidirectional carbon/epoxy samples under shear fatigue loading. 17th Int. Conf. Compos. Mater., Edinburgh, Scotland. 2009.
[66] Makeev A. Interlaminar shear fatigue behavior of glass/epoxy and carbon/epoxy composites. Compos Sci Technol 2013;80:93–100. https://doi.org/10.1016/j.compscitech.2013.03.013.
[67] Wisnom MR, Jones MI. Through thickness fatigue failure of fibre-reinforced composites. Aeronaut J 1998;102(1012):83–8. https://doi.org/10.1017/S0001924000065568.
[68] Bhasin M, Wu S, Ladani RB, Kinloch AJ, Wang CH, Mouritz AP. Improvements to the mode I fatigue resistance of epoxy nanocomposites using aligned graphene nanoplatelets. 21st Int. Conf. Compos. Mater., Xi'an, China. 2017.
[69] Maimí P, Camanho P, Mayugo J, Dávila C. A continuum damage model for composite laminates: Part I – constitutive model. Mech Mater 2007;39(10):897–908. https://doi.org/10.1016/j.mechmat.2007.03.005.
[70] Maimí P, Camanho P, Mayugo J, Dávila C. A continuum damage model for composite laminates: Part II – computational implementation and validation. Mech Mater 2007;39(10):909–19. https://doi.org/10.1016/j.mechmat.2007.03.006.
[71] Davila CG, Camanho PP, Rose CA. Failure criteria for FRP laminates. J Compos Mater 2005;39(4):323–45. https://doi.org/10.1177/0021998305046452.
[72] May M, Hallett SR. A combined model for initiation and propagation of damage under fatigue loading for cohesive interface elements. Compos Part A-Appl S 2010;41(12):1787–96. https://doi.org/10.1016/j.compositesa.2010.08.015.
[73] May M, Hallett SR. An advanced model for initiation and propagation of damage under fatigue loading – Part I: model formulation. Compos Struct 2011;93(9):2340–9. https://doi.org/10.1016/j.compstruct.2011.03.022.
[74] ABAQUS, User's Manual; 2011.
[75] Turon A, Dávila C, Camanho P, Costa J. An engineering solution for mesh size effects in the simulation of delamination using cohesive zone models. Eng Fract Mech 2007;74(10):1665–82. https://doi.org/10.1016/j.engfracmech.2006.08.025.
[76] Turon A, Camanho P, Costa J, Renart J. Accurate simulation of delamination growth under mixed-mode loading using cohesive elements: definition of interlaminar strengths and elastic stiffness. Compos Struct 2010;92(8):1857–64. https://doi.org/10.1016/j.compstruct.2010.01.012.
[77] Furtado C, Ni X, Kalfon-Cohen E, Arteiro A, Wardle BL, Camanho PP. Damage modelling of thin-ply nano-reinforced composite laminates. 21st Int. Conf. Compos. Mater., Xi'an, China. 2017.
[78] Lopes C, Camanho P, Gürdal Z, Maimí P, González E. Low-velocity impact damage on dispersed stacking sequence laminates. Part II: numerical simulations. Compos Sci Technol 2009;69(7-8):937–47. https://doi.org/10.1016/j.compscitech.2009.02.015.
[79] Bessa M. Meso-mechanical model of the structural integrity of advanced composite laminates Master's thesis Universidade do Porto, Porto, Portugal; 2010.
[80] Catalanotti G, Xavier J, Camanho P. Measurement of the compressive crack resistance curve of composites using the size effect law. Compos Part A-Appl S 2014;56:300–7. https://doi.org/10.1016/j.compositesa.2013.10.017.
[81] Catalanotti G, Arteiro A, Hayati M, Camanho P. Determination of the mode I crack resistance curve of polymer composites using the size-effect law. Eng Fract Mech 2014;118:49–65. https://doi.org/10.1016/j.engfracmech.2013.10.021.
[82] Marlett K, Ng Y, Tomblin J. Hexcel 8552 AS4 unidirectional prepreg at 190 gsm & 35% RC qualification material property data report; 2011.
[83] Makeev A, He Y, Schreier H. Short-beam shear method for assessment of stress-strain curves for fibre-reinforced polymer matrix composite materials. Strain 2013;49(5):440–50. https://doi.org/10.1111/str.12050.
[84] Berg C, Tirosh J, Israeli M. Analysis of short beam bending of fiber reinforced composites. Compos Mater Test Des (Second Conf) West Conshohocken, PA: ASTM International; 1972. p. 206–18. https://doi.org/10.1520/STP27748S.
[85] Whitney JM, Browning CE. On short-beam shear tests for composite materials. Exp Mech 1985;25(3):294–300. https://doi.org/10.1007/BF02325100.
[86] Sullivan JL, Van Oene H. An elasticity analysis for the generally and specially orthotropic beams subjected to concentrated loads. Compos Sci Technol 1986;27(2):133–55. https://doi.org/10.1016/0266-3538(86)90068-0.
[87] Leif CA, Adams DF, Pipes RB. Experimental characterization of advanced composite materials. 4th ed. CRC Press; 2014. https://doi.org/10.1201/NOE1587161001. arXiv:arXiv:1011.1669v3.
[88] Spearing SM, Sinclair I. The micro-mechanics of strength, durability and damage tolerance in composites: new insights from high resolution computed tomography. IOP Conf Ser Mater Sci Eng 2016;139(1):012007. https://doi.org/10.1088/1757-899X/139/1/012007.
[89] Garcea S, Wang Y, Withers P. X-ray computed tomography of polymer composites. Compos Sci Technol 2018;156:305–19. https://doi.org/10.1016/j.compscitech.2017.10.023.
[90] Grimmer CS, Dharan CKH. High-cycle fatigue of hybrid carbon nanotube/glass fiber/polymer composites. J Mater Sci 2008;43(13):4487–92. https://doi.org/10.1007/s10853-008-2651-9.
[91] Bortz DR, Merino C, Martin-Gullon I. Carbon nanofibers enhance the fracture toughness and fatigue performance of a structural epoxy system. Compos Sci Technol 2011;71(1):31–8. https://doi.org/10.1016/j.compscitech.2010.09.015.
[92] Kaiser AL, Stein IY, Cui K, Wardle BL. Process-morphology scaling relations quantify self-organization in capillary densified nanofiber arrays. Phys Chem Chem Phys 2018;20(6):3876–81. https://doi.org/10.1039/C7CP06869G.

SUPPLEMENTARY MATERIALS

Static and fatigue interlaminar shear reinforcement of aligned carbon nanotube-reinforced hierarchical advanced composites

Xinchen Ni[a], Carolina Furtado[c,d], Estelle Kalfon-Cohen[b], Yue Zhou[a], Gabriel A. Valdes[b], Travis J. Hank[2], Pedro P. Camanho[c,d], Brian L. Wardle[b]

[a] *Department of Mechanical Engineering, Massachusetts Institute of Technology, Cambridge, MA 02139 USA*
[b] *Department of Aeronautics and Astronautics, Massachusetts Institute of Technology, Cambridge, MA 02139 USA*
[c] *DEMec, Faculdade de Engenharia da Universidade do Porto, Rua Dr. Roberto Frias, s/n, 4200-465 Porto, Portugal*
[d] *INEGI, Instituto de Ciência e Inovação em Engenharia Mecânica e Engenharia Industrial, Rua Dr. Roberto Frias, 400, 4200-465 Porto, Portugal*

Figure S1 shows the cross-sections of aligned carbon nanotube (A-CNT) forest transferred on an uncured prepreg ply, confirming that the alignment is maintained during the transfer process, while preserving the original ~20µm height. This observation is consistent with prior work[1].

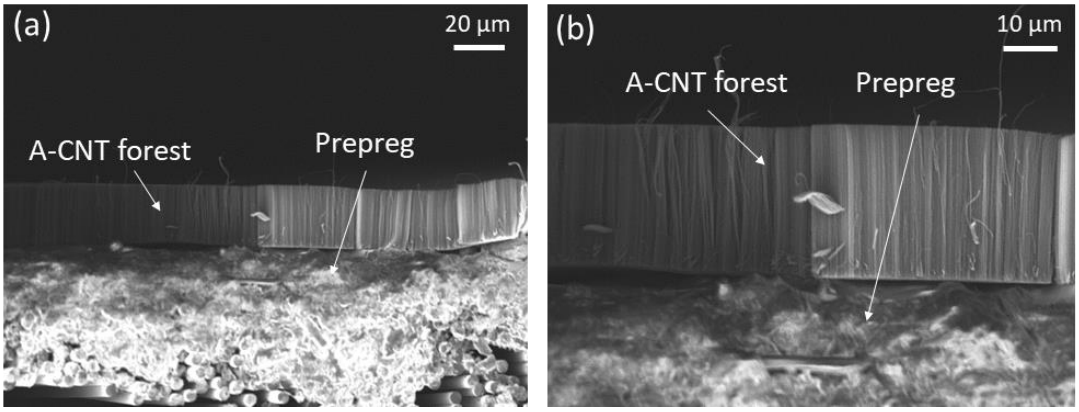

Figure S1: Scanning electron micrographs at two magnifications of an aligned carbon nanotube (A-CNT) forest after it was transferred onto an uncured prepreg showing that the alignment is preserved.

Figure S2 shows representative load-displacement curves for both baseline and nanostitched specimens. After settling, both specimens exhibit linear-elastic behaviour until a sudden load drop indicating a brittle type of failure with little evidence of accumulated damage except for a slight softening.

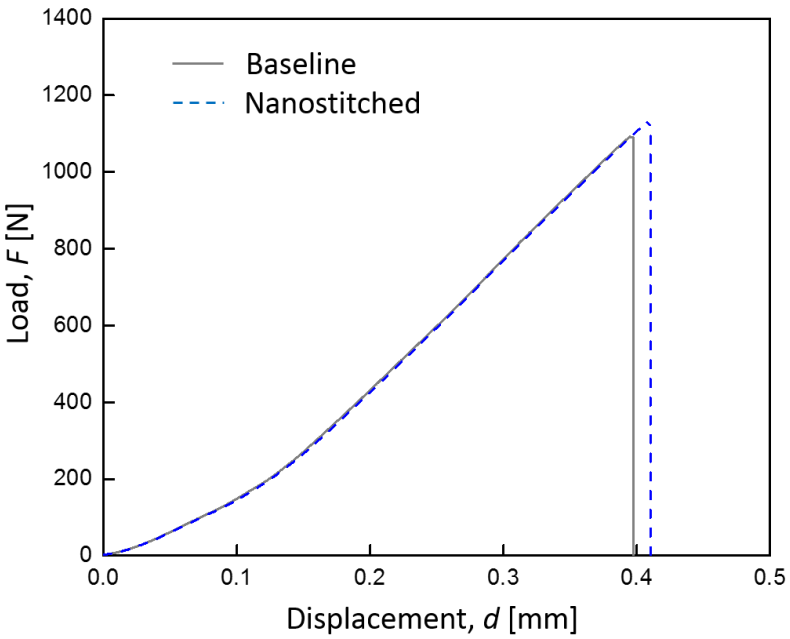

Figure S2: Representative load-displacement curves for static short-beam shear (SBS) test.

Figure S3 shows a representative compliance history plot for both baseline and nanostitched specimens. All specimens showed a sudden increase in compliance regardless of whether they failed catastrophically or via the displacement criteria. Table S1 provides the fatigue life values at the different loading levels, with outliers removed per the modifed Thompson tau criterion using [2].

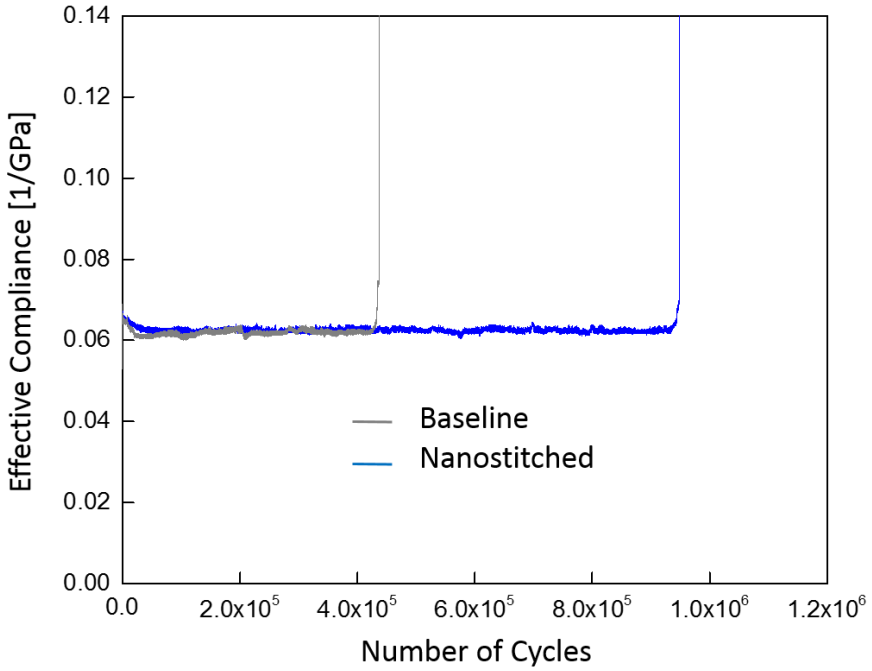

Figure S3: Represensative effective compliance vs. number of cycles in SBS fatigue test.

Table S1: Fatigue life via SBS for baseline and nanostitched specimens across all load levels (60 to 90% of static strength), and fatigue life increase percentage due to nanostitching.

Load level	Baseline specimen fatigue life (cycle)	Nanostitched specimen fatigue life (cycle)	Fatigue life increase (%)
90%	164±37	253±21	54
80%	1,182±190	2,358±199	100
70%	14,514±3,067	22,844±4,672	57
60%	254,961±182,649	889,099±59,157	249
50%	603,156±231,666	NA	NA

References

[1] E. Kalfon-Cohen, R. Kopp, C. Furtado, X. Ni, A. Arteiro, G. Borstnar, M.N. Mavrogordato, I. Sinclair, S.M. Spearing, P.P. Camanho, B.L. Wardle, Synergetic effects of thin plies and aligned carbon nanotube interlaminar reinforcement in composite laminates, Compos. Sci. Technol. 166 (2018) 160–168.

[2] A.J. Wheeler, A.R. Ganji, Introduction to Engineering Experimentation, 3rd Ed., Pearson Higher Education, c2010., Upper Saddle River, N.J., 2010.